JCTC Journal of Chemical Theory and Computation

Toward an Accurate Density-Functional Tight-Binding Description of Zinc-Containing Compounds

Ney H. Moreira,* Grygoriy Dolgonos, Bálint Aradi, Andreia L. da Rosa, and Thomas Frauenheim

Bremen Center for Computational Materials Science, University of Bremen, Am Fallturm 1, 28359 Bremen, Germany

Received October 28, 2008

Abstract: An extended self-consistent charge density-functional tight-binding (SCC-DFTB) parametrization for Zn−X (X = H, C, N, O, S, and Zn) interactions has been derived. The performance of this new parametrization has been validated by calculating the structural and energetic properties of zinc solid phases such as bulk Zn, ZnO, and ZnS; ZnO surfaces and nanostructures; adsorption of small species (H, CO_2, and NH_3) on ZnO surfaces; and zinc-containing complexes mimicking the biological environment. Our results show that the derived parameters are universal and fully transferable, describing all the above-mentioned systems with accuracies comparable to those of first-principles DFT results.

1. Introduction

Zinc is the second most abundant transition metal in living organisms, playing an important role in many biological processes as a part of metalloenzymes or complexes with amino acids, nucleic acids, or proteins. Additionally, zinc oxide (ZnO) is a promising material for applications in electronics and optoelectronics, since it is a wide band gap semiconductor and has large excitonic binding energy. Recently, ZnO has been synthesized in a variety of nanostructures, including nanowires,[1−3] nanobelts,[4−6] nanorods,[7,8] and nanopilars,[9,10] which opens up the possibility for novel applications. Furthermore, the covalent attachment of functional organic linkers to ZnO surfaces can be used in biosensing applications.[11]

Zinc-containing systems have been widely investigated by first-principles methods.[12,13] Although such methods represent the state-of-the-art approach in materials science and solid-state simulations, they become prohibitive at treating a large number of atoms because of their high computational demands. In this context, one of the most promising approaches is the self-consistent charge density-functional tight-binding[14,15] (SCC-DFTB) method, which has been successfully applied to large-scale quantum-mechanical simulations in solid-state physics, chemistry, materials science, and biophysics.[16,17] The method is an approximation to the Kohn−Sham density-functional theory (DFT),[18] which combines reasonable accuracy and computational efficiency. However, the limited set of available parameters is still a drawback, and in some cases the transferability of parameters between solid and molecular environments is still a problem. For example, a recent SCC-DFTB parametrization for Zn has been successfully applied to investigate zinc-containing biological molecules,[19] but this set has been unable to model solid-phase zinc systems with acceptable accuracy.

It becomes evident that a new SCC-DFTB parametrization for zinc interactions, able to describe both solid-state and biological systems, would open up new possibilities for investigating Zn-containing materials. Further, it would reinforce the confidence in the transferability of SCC-DFTB parameters among different environments.

In this work, we present our recently derived SCC-DFTB parametrization for representing zinc and its interactions with hydrogen, carbon, nitrogen, oxygen, and sulfur. The parametrization has been validated by comparing SCC-DFTB results with literature data for solid-state zinc-containing systems (metallic Zn, ZnO in the wurzite (w), and ZnS in the zinc-blend (zb) structures), ZnO surfaces and nanostructures, adsorption of small species (H, CO_2, and NH_3) on ZnO, and models for zinc biological complexes. Our results have been found quantitatively comparable to those obtained by DFT calculations, demonstrating that the derived parameters

* Corresponding author e-mail: henrique.ney@bccms.uni-bremen.de.

10.1021/ct800455a CCC: $40.75
Published on Web 02/06/2009

are reliable in predicting geometries and energetics of both solid and molecular systems, being fully transferable among different chemical environments.

2. Computational Methodology

2.1. SCC-DFTB Method. Since the foundations of the DFTB approach are described elsewhere[14,15] and have been also the subject of a recent review,[20] only a short description of the method will be given here.

The SCC-DFTB total energy expression (eq 1) is a second-order expansion of the DFT Kohn−Sham total energy with respect to charge density fluctuations (δn):

$$E_{\mathrm{tot}}^{\mathrm{DFTB}} = \sum_{i}^{\mathrm{occ}} n_i \langle \Psi_i | \hat{H}_0 | \Psi_i \rangle + \frac{1}{2} \sum_{\alpha\beta}^{N} \gamma_{\alpha\beta} \Delta q_\alpha \Delta q_\beta + E_{\mathrm{rep}} = E_0[n_0] + E_2[n_0, \delta n] + E_{\mathrm{rep}} \quad (1)$$

In this expression, the zero-order term E_0 is the energy summation over all occupied eigenstates Ψ_i. The approximated non-SCC Hamiltonian ($\hat{H}_0$) is derived within the two-center approximation for an arbitrary reference charge density (n_0), introduced as the superposition of individual atomic charge densities. This Hamiltonian is also subjected to the frozen-core approximation (i.e., only the valence electrons are considered explicitly and the inner electrons are represented by an effective (pseudo) potential). The second term E_2 corresponds to the second-order expansion of the exchange-correlation functional with respect to the charge density fluctuations δn (the first-order terms in this expansion vanish for any arbitrary n_0), approximated as atomic pointlike charges (Δq). Finally, the third term E_{rep} accounts for the "double-counting" terms and the ion−ion core interactions in a set of distance-dependent pairwise repulsive potentials, modeled as the difference between the SCC-DFTB electronic energy ($E_{\mathrm{Elec}}^{\mathrm{DFTB}} = E_0 + E_2$) and the total DFT energy for some reasonably chosen reference system:

$$E_{\mathrm{rep}} = \sum_{\alpha,\beta} U_{\alpha\beta}(R_{\alpha\beta}) \quad (2)$$

where

$$U_{\alpha\beta}(R_{\alpha\beta}) = E_{\mathrm{Total}}^{\mathrm{DFT}}(R_{\alpha\beta}) - E_{\mathrm{Elec}}^{\mathrm{DFTB}}(R_{\alpha\beta})$$

with $R_{\alpha\beta}$ representing the distance between the atoms α and β.

The wave functions (Ψ_i) are expanded as a linear combination of atomic orbitals:

$$\Psi_i = \sum_{\mu} c_\mu \phi_\mu \quad (3)$$

In the common DFTB framework, the atomic orbitals (ϕ) in eq 3 are constructed as linear combinations of Slater-type orbitals, obtained by solving self-consistently the modified Kohn−Sham equation (eq 4) for the spin-unpolarized free atom:

$$\left[\hat{T} + w^0 + \left(\frac{r}{r_0}\right)^2\right] \phi_\mu(r) = \varepsilon_\mu \phi_\mu(r) \quad (4)$$

The modified Hamiltonian in eq 4 consists of a kinetic energy operator $\hat{T}$, the potential energy for the neutral atom w^0, and an additional harmonic potential $(r/r_0)^2$ used to enforce the localization of the atomic orbitals and to improve the quality of energy band structures (see ref 20 for details).

Having defined the atomic orbitals (ϕ) and an initial set of expansion coefficients (c_μ), we estimated the atomic charge fluctuations (Δq) via Mulliken population analysis, and the DFTB total energy problem is solved self-consistently by using the secular eq 5

$$\sum_i c_{i\mu}(H_{\mu\nu} - \varepsilon_i S_{\mu\nu}) = 0 \quad \forall \mu, i \quad (5)$$

with

$$H_{\mu\nu} = H_{\mu\nu}^0 + \frac{1}{2} S_{\mu\nu} \sum_{\xi}^{N} (\gamma_{\alpha\xi} + \gamma_{\beta\xi}) \Delta q_\xi$$

$$H_{\mu\nu}^0 = \langle \phi_\mu | \hat{H} | \phi_\nu \rangle \quad \forall \mu \in \alpha, \nu \in \beta$$

$$S_{\mu\nu} = \langle \phi_\alpha | \phi_\nu \rangle$$

In eq 5, the diagonal zero-order matrix elements $H_{\mu\nu}^0$ are taken as the eigenvalues obtained from the free-atom calculations, while the distance-dependent nondiagonal elements $H_{\mu\nu}^0$ and $S_{\mu\nu}$ are calculated within the two-center approximation and tabulated for all future calculations. This procedure avoids integral evaluations during the DFTB calculation, leading to a computational efficiency comparable to those of traditional semiempirical methods while retaining the accuracy comparable to those of DFT methods. The charge transfers among different atoms take into account their respective chemical hardnesses (Hubbard parameters), calculated as the first derivative of the total atomic energy with respect to the electronic occupation around the neutral-atom electronic density.

2.2. Parametrization Details. The parameters necessary to represent a system within the DFTB method include the Hubbard parameters for every chemical element, the $H_{\mu\nu}^0$ and $S_{\mu\nu}$ matrix elements, and the repulsive pairwise potentials for all interacting neighbors. Fortunately, all of these parameters are controlled by a few main quantities to be determined in the parametrization process, namely: (i) the reference input density (n_0), (ii) the wave function confinement radius (r_0), and (iii) the repulsive cutoffs, determining the distances where the repulsive pairwise potentials (E_{rep}) vanish.

As the parametrization reported here extends a previous well-established one,[21] all parameters not involving zinc atoms are assumed to be the same as in ref 19, including n_0 and r_0 for the H, C, N, O, and S atoms. For zinc, n_0 was confined into a 2.69 Å radius while r_0 was chosen to be 1.59 Å, because these values provided a good compromise among the description of geometries, cohesive properties, and electronic band structures for hexagonal closed-packed (hcp)-Zn and w-ZnO structures. The reference systems and cutoffs used to model the Zn−X (X = H, C, N, O, S, and Zn) pairwise repulsive potentials are summarized in Table 1.

The electronic DFTB parameters (i.e., Hubbard parameters, $H_{\mu\nu}^0$ and $S_{\mu\nu}$ matrix elements) were derived directly from DFT calculations, performed within the generalized gradient

Table 1. Parametrization Details of the Pairwise Repulsive Potentials for Zn−X Interactions (X = H, C, N, O, S, and Zn)[a]

interaction	reference system	repulsive cutoff (Å)	equilibrium Zn−X distance (Å)	
			SCC-DFTB	DFT
Zn−H	ZnH_2	1.63	1.63	1.54
Zn−C	$Zn(CH_3)_2$	2.01	1.97	1.95
Zn−N	$Zn(NH_3)_2$	2.10	1.92	1.95
Zn−O	zb-ZnO	2.23	2.00	1.98
Zn−S	$Zn(SH)_2$	2.40	2.21	2.17
Zn−Zn	fcc-Zn	2.75	2.79	2.74

[a] fcc = face-centered cubic.

approximation (GGA) and using the Perdew, Burke, and Ernzerhof (PBE)[22] exchange-correlation functional. All parameters derived here are available for use by the scientific community and can be downloaded from http://www.dftb.org/parameters/ (search for the set named "znorg-0-1").

2.3. Reference DFT Calculations. In the DFT reference calculations to derive the Zn−X repulsive potentials ($U_{\alpha\beta}$), we employed the GGA/PBE functional (for X = H, C, O, and Zn), as implemented in the SIESTA package[23] using a double-ζ plus polarization function (DZP) basis set and norm-conservative Troullier−Martins pseudo-potentials[24] (PP) for representing the valence and inner electrons, respectively. The Becke three-parameter, Lee, Yang, and Parr (B3LYP) hybrid functional[25,26] in conjunction with the 6-311G+(d, p) basis set, as implemented in the Gaussian03 package,[27] was used for X = N, S.

All GGA/PBE calculations were performed with periodic boundary conditions (PBC). For the fcc-Zn and zb-ZnO solid-state reference systems, the *k*-points were sampled with a (8 × 8 × 8) Monkhorst−Pack[28] (MP) grid. For molecular reference systems, the calculations were performed by employing large supercells, including a 25 Å vacuum region in all directions to isolate the molecules from their periodic replicas.

2.4. SCC-DFTB Calculations. The SCC-DFTB calculations were performed with the DFTB+ code.[29] Solid-state hcp-Zn, w-ZnO, and zb-ZnS properties were calculated using PBC and converged (8 × 8 × 4), (8 × 8 × 4), and (8 × 8 × 8) MP *k*-points, respectively. The calculations for ZnO surfaces (clean and with small adsorbates) were performed using suitably oriented supercells and PBC within the slab approach.[39] A vacuum region of 25 Å along the surface-normal direction and a (4 × 4 × 1) MP grid for the *k*-point sampling were employed. The [0001] ZnO nanostructures had their growth direction oriented along the *z*-axis in the supercell, with vacuum regions of 25 Å along the *x* and *y* directions, and were calculated using a (1 × 1 × 4) MP grid for *k*-point sampling. To mimic the zinc environment in biomolecules, we performed geometry optimizations of small zinc-containing complexes, as suggested by Elstner et al.[19] In all SCC-DFTB calculations, the atomic positions were relaxed until the forces in the system became smaller than 0.001 eV/Å.

Table 2. Selected hcp-Zn and w-ZnO Bulk Properties Calculated with SCC-DFTB and DFT Methods and Obtained from Experiments[h]

	E_{coh} (eV)	*a* (Å)	*c* (Å)	*V* (Å^3)	B_0 (GPa)	B_0'
			hcp-Zn			
SCC-DFTB[a]	2.45	2.71	5.04	32.20	114	5.67
PP-DZP/PBE[a]	1.92	2.68	5.00	31.24	73	5.93
PP-PW/PW91[b]		2.65	5.10	31.02	60	6.59
expt	1.36[c]	2.61[b]	4.91[b]	28.96[b]	60−80[b]	5.2−6.4[b]
			w-ZnO			
SCC-DFTB[a]	9.77	3.28	5.25	50.04	161	2.49
PP-DZP/PBE[a]	8.08	3.30	5.34	51.08	124	4.55
PP-PW/PBE[d]	8.98	3.34	5.30	51.40	171	
expt[e]	7.52	3.25	5.20	47.62	208	4
			zb-ZnS			
SCC-DFTB[a]	7.93	5.43		160.1	44.2	2.4
PP-PW/LDA[f]	7.22	5.35		153.3	82	4.6
PP-PW/PW91[g]		5.60		175.6	66.7	3.95
expt[f]	6.33	5.40		157.5	76.9	4.9

[a] GGA/PBE calculation performed with the SIESTA package; this work. [b] GGA/PW91 (Perdew−Wang 1991 exchange-correlation functional) calculation in ref 32. [c] Reference 33. [d] GGA/PBE calculation in ref 34. [e] Reference 35. [f] LDA calculation in ref 36. [g] GGA/PW91 (Perdew−Wang 1991 exchange-correlation functional) calculation in ref 37. [h] PW = plane-wave basis set.

3. Results and Discussion

3.1. Bulk Systems. The bulk hcp-Zn, w-ZnO, and zb-ZnS lattice parameters and elastic properties were determined by calculating energy-volume profiles in a ±15% range around the experimental equilibrium volumes and fitting the results to the Murnaghan equation of state. For hcp-Zn and w-ZnO structures, we fixed the experimental *c*/*a* ratios (1.630[30] and 1.602,[31] respectively).

As shown in Table 2, the DFTB parameters for all considered bulk systems are in fairly good agreement with DFT and experimental ones. The deviations in the cohesive energies are not surprising, since DFTB calculations usually overestimate this property,[38] while the error in the Zn bulk modulus is a consequence of strong zinc wave function compression applied to this element (∼1.3 times larger than the Zn covalent radius), which shortens its dissociation bond distances and lowers its electronic energy wells. Nevertheless, this strong wave function compression ensures reasonable band structures for the solid materials, as exemplified in Figure 1 for the case of w-ZnO.

It should be mentioned that, because of the small basis set employed, the energy band structures calculated with DFTB are not in the same way affected by the band gap problem, as observed in local density approximation (LDA) and GGA calculations. Therefore, with no additional correction scheme being applied, the ZnO band gap obtained via DFTB (∼4.1 eV) is closer to the experimental value (∼3.3 eV) than the GGA-PBE result (∼0.9 eV). It may be taken as an advantage to study electronic states introduced by defects or adsorbed species; however, it must be noted that the dispersions in the edge of the conduction band are considerably smaller than those found in GGA-PBE results and may lead to deviations in calculating transport properties.

Concerning the hcp-Zn and w-ZnO cohesive energies, the overestimation in principle could be corrected by applying

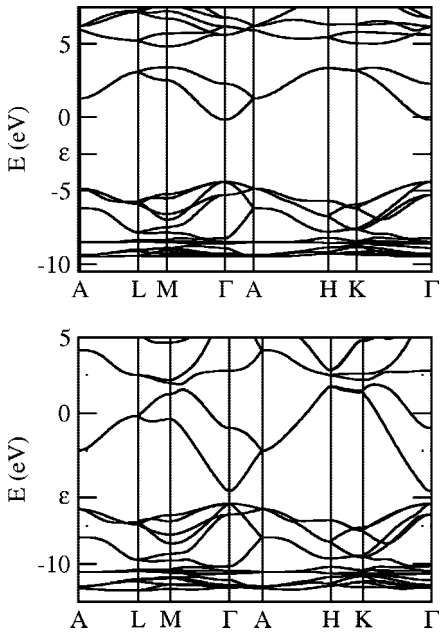

Figure 1. Electronic band structures for w-ZnO calculated with SCC-DFTB (top) and DFT (PP-DPZ/PBE) (bottom) methods. The DFT band structure was calculated using the SIESTA package. ε denotes the Fermi level for each case.

longer repulsive potentials, slightly sacrificing the geometrical parameters. However, we verified that this procedure leads to wrong relaxations for ZnO surfaces and nanostructures, where the outermost atoms move toward the vacuum region to avoid the artificially enhanced repulsion.

3.2. ZnO Surfaces. ZnO surfaces form a good probe set to test the new parameters, since they have the bulk symmetry broken along one direction. Additionally, they have been subject to several DFT studies in the literature.[39,40] The (10$\underline{1}$0), (1$\underline{2}$10), (0001/000$\underline{1}$), and depolarized dep-(0001) surfaces were constructed starting from the equilibrium DFTB w-ZnO structure. The surface unit cells for these four structures are represented in Figure 2. In all cases, our results for the surface relaxations are in good agreement with those reported in ref 40, as shown in Table 3.

The relaxations in the (10$\underline{1}$0) terminated slabs (Figure 3A) are only significant in the three outermost surface layers. The oxygen atoms remain close to their bulk positions, while the zinc atoms move inward in the top layer and slightly outward in the second layers. In comparison with the bulk values, the bond lengths between the top and the second layer, d_{Zn-O}, are ~6% shortened while the bonds between the second and the third layers are ~3% larger. The O−Zn−O angle (α) changes from its 109° bulk value to 117° at the top surface layer, remaining unchanged in the inner layers. The (1$\underline{2}$10)-terminated slabs follow similar trends, with relaxations observed especially over the outermost Zn atoms, leading to a ZnO bond length ~4% shorter and strongly distorted bond angles at the surface.

The depolarized (0001) surface relaxation, as shown in Figure 4B, agrees well not only with the theoretical prediction derived by Claeyssens et al.,[40] but also with recent experimental data confirming the existence of such structure in ZnO ultrathin films.[41] This is a graphite-like structure, where both O and Zn atoms assume a planar sp^2 configuration, with all

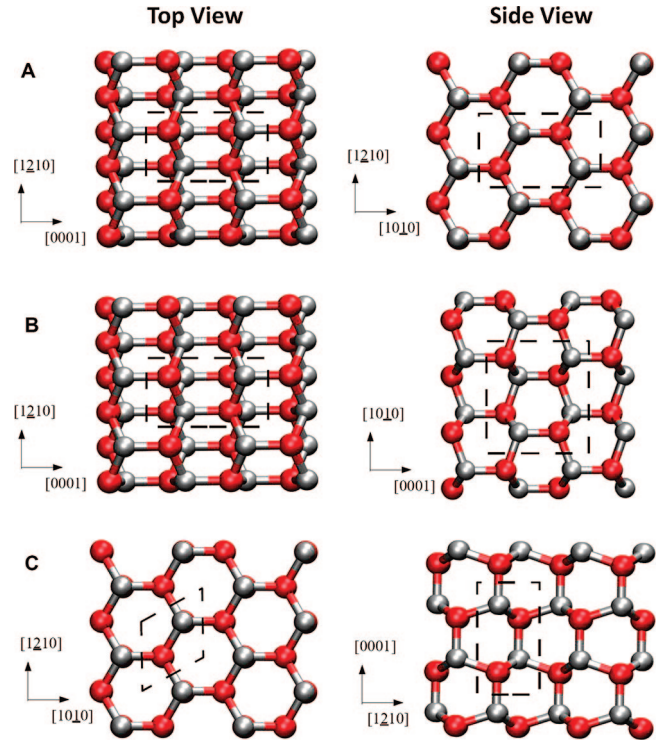

Figure 2. Top and side views of surface unit cells for (10$\underline{1}$0) (A), (1$\underline{2}$10) (B), and (0001/000$\underline{1}$) (C) surfaces. The dep-(0001) surface unit cell is similar to that used for its polar counterpart, but with planar ZnO sheets perpendicular to the [0001] direction.

Table 3. Comparison of Geometrical Relaxations in ZnO Surfaces Calculated with DFTB, for Selected Structural Parameters As Specified in Figures 3 and 4, with DFT (PP-PW/PW91) Results in Ref 40

		surface layers		inner layers	
surface	parameter	SCC-DFTB	PP-PW/PW91	SCC-DFTB	PP-PW/PW91
ZnO(10$\underline{1}$0)					
	d_{Zn-O} (Å)	1.88	1.85	2.01	1.99
	d'_{Zn-O} (Å)	2.05	2.06	2.01	1.99
	α (deg)	117	117	109	
	β (deg)	108		109	
ZnO(1$\underline{2}$10)					
	d_{Zn-O} (Å)	1.93	1.87	2.01	1.99
	d_{O-Zn} (Å)	2.00	1.96	2.01	1.99
	d'_{Zn-O} (Å)	2.05	2.06	2.01	
	α (deg)	118	117	109	
	β (deg)	97		109	
ZnO(0001/000$\underline{1}$)					
	d_{Zn-O} (Å)	1.94	1.92	1.99	1.97
	d'_{Zn-O} (Å)	2.08	2.15	2.05	2.08
	α (deg)	111	113	109	
	β (deg)	120	120	90	
ZnO (dep-0001)					
	d_{Zn-O} (Å)	1.90	1.93	1.90	
	d'_{Zn-O} (Å)	2.34	2.4	2.34	
	α (deg)	120	120	120	
	β (deg)	90		90	

in-plane bonds by ~3% smaller than those in the w-ZnO, and with large interlayer distances (~2.34 Å). In this case, the relaxations do not differ significantly among different layers into the slab and are also not influenced by the slab

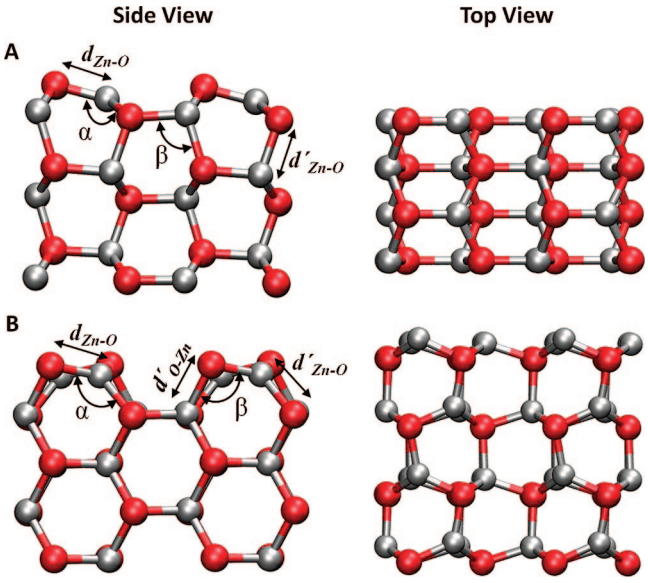

Figure 3. Side and top views of the first three bilayers of relaxed (10$\underline{1}$0) (A) and (1$\underline{2}$10) (B) ZnO surfaces calculated with SCC-DFTB.

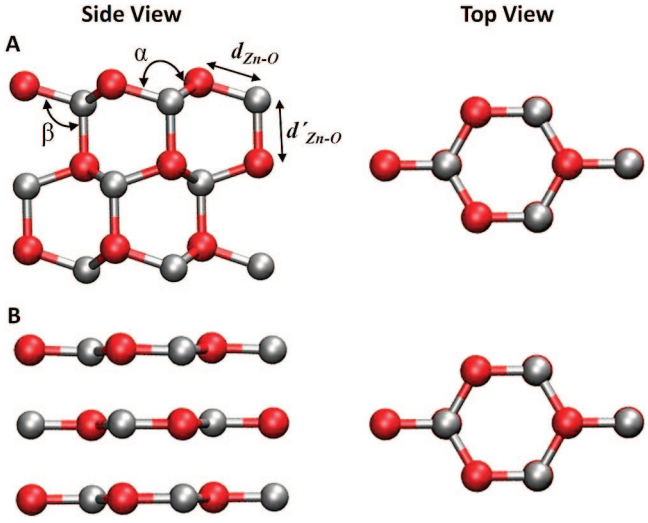

Figure 4. Side and top views of (A) the relaxed (0001/000$\underline{1}$) and (B) dep-(0001) ZnO surfaces calculated with SCC-DFTB.

thickness. For the polar (0001/000$\underline{1}$) surface, where the structure resembles the w-ZnO (Figure 4A) one, the relaxations extend through the whole slab and are more sensitive to variations in its thickness. Further, we also observed small charge transfers from the oxygen-terminated to the zinc-terminated surface (~0.3e per slab unit cell), which have usually been considered as a stabilizing mechanism for such surfaces.[42,43]

Since the polar (0001) and (000$\underline{1}$) surfaces are not equivalent, it is not possible to calculate their absolute formation energies. Therefore, we calculated the cleavage energy (the energy required to create two surfaces by cleaving the perfect crystal) for all calculated slabs to verify their relative stability as a function of the film thickness (Figure 5). The results are in excellent agreement with the DFT predictions in ref 40. As expected, the slabs with the polar surfaces are less stable than those (10$\underline{1}$0)- and (1$\underline{2}$10)-

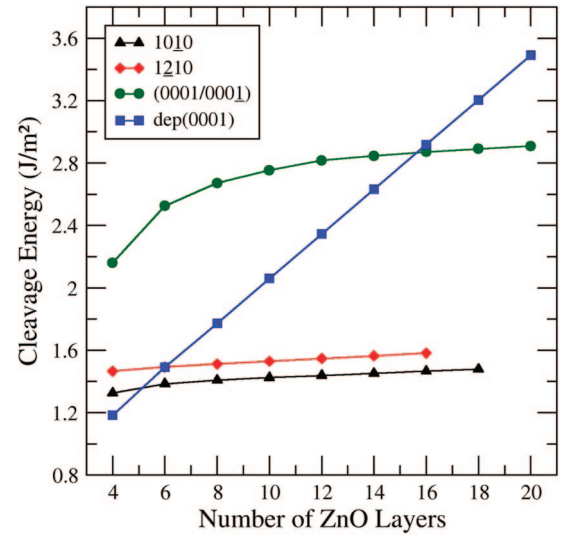

Figure 5. SCC-DFTB cleavage energy for (10$\underline{1}$0), (1$\underline{2}$10), (0001/000$\underline{1}$), and dep(0001) ZnO surfaces as a function of the slab thickness.

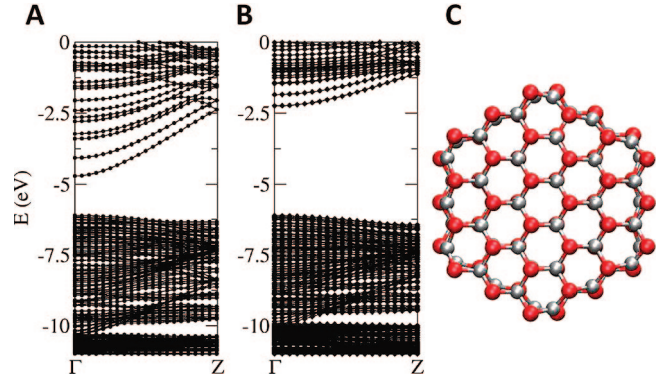

Figure 6. (A) DFT (PP-DPZ/PBE) and (B) SCC-DFTB electronic band structures for (C) the hexagonal [0001] nanowire with a diameter of 16.5 Å. The DFT calculation was performed using the SIESTA package.

terminated. However, the (0001) depolarized structure is the most stable for the thinnest films, in accordance with the one experimentally found for ultrathin ZnO films,[41] but quickly rising in energy with increasing the slab thickness. It is necessary to remark that the phase transitions from the depolarized (0001) film to other configurations (in this study, at 5-, 6-, and 16-layer-thick slabs, respectively) take place at points slightly different from those found by Claeyssens et al. (namely, 9, 10, and 18 layers), but this does not affect the general conclusions drawn here.

3.3. ZnO Nanostructures. To extend the validation procedure to ZnO nanostructures, we investigated (10$\underline{1}$0)-faceted hexagonal nanowires with different diameters (3.7, 9.9, 16.5, and 23.0 Å, respectively). Figure 6 shows the relaxed cross section of one of the investigated nanowires and its band structure calculated with both DFT and DFTB. For all nanowires, the relaxations at the outermost layers follow the same general trends observed for the (10$\underline{1}$0) surfaces, being also in very good agreement with previous DFT results.[42] The inner atoms remain close to their positions in the bulk ZnO, as the O atoms at the surface, whereas the zinc atoms at the surface move inward, shrinking the distance

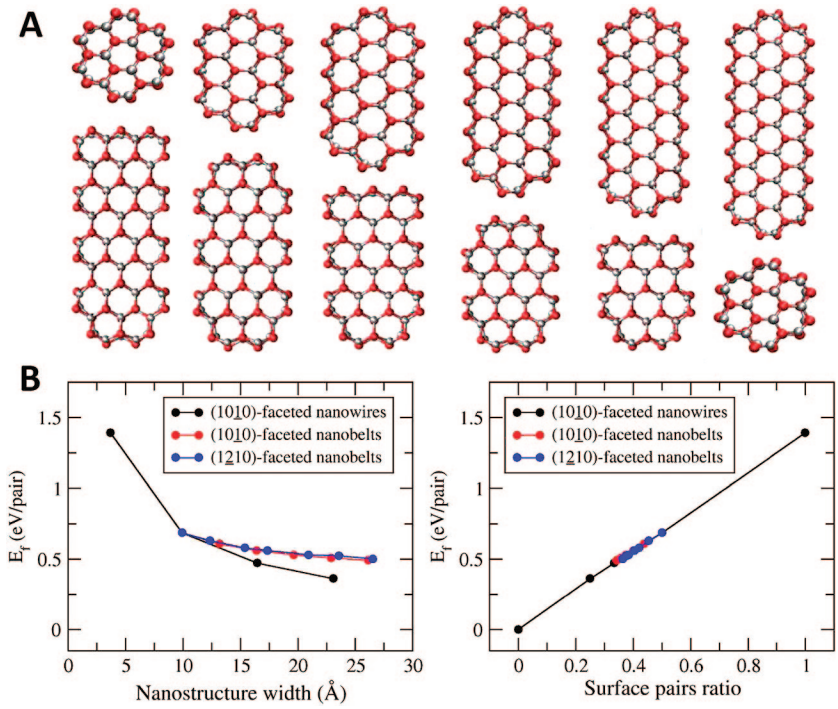

Figure 7. (A) Cross section of the relaxed structure for (10$\bar{1}$0)- (top) and (12$\bar{1}$0)-faceted (bottom) [0001] ZnO nanobelts with different widths across the dominating surface calculated with SCC-DFTB. (B) Formation energies of ZnO nanostructures grown along the [0001] direction, for hexagonal nanowires, (10$\bar{1}$0)- and (12$\bar{1}$0)-faceted nanobelts, as a function of the nanostructure width and surface pair ratio.

to their nearest inner Zn neighbors to 3.07 Å. The exception is the smallest nanowire, where the relaxations are more pronounced, with 2.86 Å as the minimal distance between Zn atoms. For these wires, the energy band structures along the Γ-Z direction in the Brillouin zone appeared in good agreement with DFT results,[42] with a direct band gap at the Γ-point, which shrinks from 4.1 to 3.6 eV as the nanowire diameter increases, indicating quantum confinement effects.

The relative stability of the nanowires is also in good agreement with plane waves calculations by Xu et al.,[12] who also demonstrated that for hexagonal nanowires the formation energy depends linearly on the ZnO surface pair ratio. To further validate the parameters, we calculated [0001]-oriented ZnO nanobelts and found a similar linear dependence, as shown in Figure 7. The nanobelts were found to have their relaxations consistent with those observed for their dominant surfaces, with their stabilities lying between that of the corresponding nanowire and that of the infinite thin film. It should be noted that the relative stability of the nanobelts increases with their width, as expected.

3.4. Adsorption of Small Molecules on ZnO Surfaces. The results achieved in describing ZnO surfaces encouraged us to start validating our parametrization for the Zn−H, Zn−C, and Zn−N interactions by investigating the adsorption of small species (atomic H, NH_3, and CO_2) on the (10$\bar{1}$0) ZnO. We analyzed their geometrical configurations on the surface and also their adsorption energies, defined as $E_{ads} = (E_T - E_{ZnO-10\bar{1}0} - n\mu)/2$, where E_T is the ZnO−adsorbate complex total energy, $E_{ZnO-10\bar{1}0}$ is the energy of the bare slab, μ is the adsorbate chemical potential, and n is the number of adsorbed species. The factor $^1/_2$ is used because we have two equivalent surfaces.

Table 4. Comparison between SCC-DFTB and B3LYP/6-311+G(d,p) Results[43] for Hydrogen Monolayer Adsorption on ZnO (10$\bar{1}$0) Surface[a]

	SCC-DFTB	B3LYP
E_{ads} (eV)	−0.77	−0.62
r(Zn−H) (Å)	1.74	1.59
r(O−H) (Å)	0.99	0.99
θ(Zn−H) (deg)	31	41
θ(O−H) (deg)	28	38

[a] The angle θ represents the inclinations of the X−H bond (X = Zn or O) to the surface normal direction.

For the H-covered surfaces, we used the hydrogen chemical potentials equal to $^1/_2$ H_2 total energy. In accordance with ab initio investigations,[43−45] our results suggest that the Zn−H bond is less energetically favorable, as the half-monolayer coverage was found to be ∼1 eV more stable than the monolayer. In both cases, the SCC-DFTB E_{ads} is slightly overestimated in comparison with first-principles results. The surface geometry for the monolayer coverage is also in reasonable agreement with the B3LYP predictions (Table 4).

For the CO_2-covered surfaces, the DFTB results (Figure 8) are in good agreement with recent DFT ones,[46] which show a tridentate surface carbonate (TSC) as the stable adsorbate species in the activation of CO_2 over ZnO. By using the CO_2 chemical potential as a variational parameter,[47] we obtained a phase-stability diagram similar to that proposed in ref 46. It should be noted that our E_{ads} values are overestimated by ∼0.5 eV per CO_2 molecule in comparison to those from ref 46. This deviation is not surprising, since our model overestimates the Zn−O bond strength in comparison with those from DFT (Table 2). Therefore, the DFTB

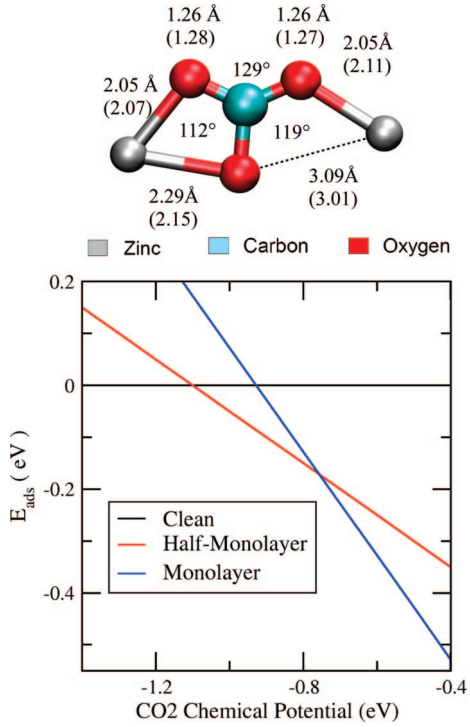

Figure 8. Top: Geometry of the TSC structure calculated with SCC-DFTB. The bond length values in the parentheses are DFT results taken from ref 46. The angles calculated with DFTB coincide exactly with those reported in ref 46. Bottom: Phase-stability diagram calculated with SCC-DFTB for different coverages of CO_2 on ZnO (10$\underline{1}$0) surfaces.

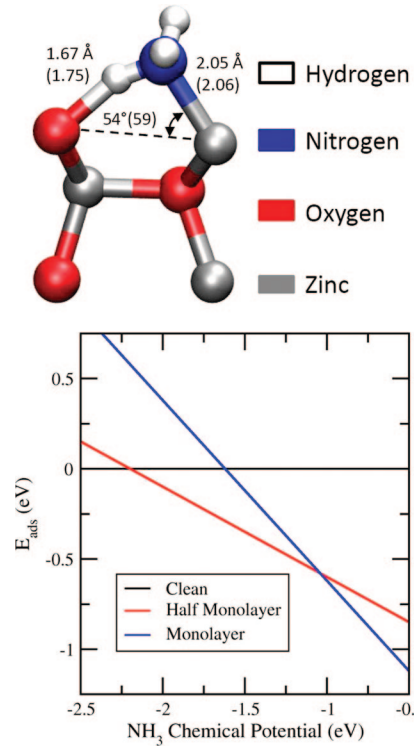

Figure 9. Top: Geometry of the H_3N-ZnO surface complex calculated with SCC-DFTB. The values in the parentheses are ab initio results taken from ref 49. Bottom: Phase-stability diagram calculated with SCC-DFTB for different coverages of NH_3 on ZnO (10$\underline{1}$0) surfaces.

adsorption energy related to the TSC structure is also overestimated in comparison with those from DFT, and the DFTB phase diagram is shifted toward lower CO_2 chemical potentials consequently. It is interesting to observe that the interaction with the CO_2 molecule strongly influences the surface geometry by pushing the Zn atoms outward and decreasing the angle α to 89° and increasing the ZnO dimer distance d_{Zn-O} to 2.29 Å.

ZnO has been also considered as a promising material for sensing NH_3 in gas phase,[48] but there are only a few theoretical studies on the absorption of ammonia on ZnO surfaces,[49] in which cluster models were employed to investigate single-molecule adsorption. A strong binding energy (∼1.8 eV)[49] was reported for the H_3N-ZnO surface complex, which is not surprising given the basicity of NH_3 and the acidic character of zinc in ZnO. This strong binding energy and the small molecular volume of ammonia in comparison to CO_2 indicate that adsorption of NH_3 on ZnO(10$\underline{1}$0) surfaces can also lead to the formation of self-assembled monolayers.

Our results show that ammonia binds to the ZnO surface through a covalent N−Zn bond (2.05 Å), thus reducing the angle α to 115° and increasing the ZnO dimer distance d_{Zn-O} to 1.96 Å. As expected, no ammonia dissociation was found. Instead, there is a typical hydrogen bond distance of 1.68 Å between ammonia hydrogen and ZnO oxygen. The NH_3 tilting angle with respect to the surface normal of 41° is in fairly good agreement with near-edge X-ray fine-structure spectroscopy reported by Kamada et al.[50] Additionally, our results (cf. Figure 9) agree very well with coupled-cluster calculations by Taft et al.[49]

Table 5. Comparison between SCC-DFTB and B3LYP/6-311+G(d,p) Cohesive Energies and Equilibrium Geometries for Zinc Complexes Containing NH_3 and HS^- Ligands

	E_{coh} (eV)		bond length (Å) (Zn−X)		bond angles (deg) (X−Zn−X)	
species	SCC-DFTB	B3LYP	SCC-DFTB	B3LYP	SCC-DFTB	B3LYP
			Zn−N			
$[ZnNH_3]^{2+}$	5.36	5.98	1.93	1.97		
$[Zn(NH_3)_2]^{2+}$	11.86	10.70	1.92	1.95	180	180
$[Zn(NH_3)_3]^{2+}$	13.96	13.34	1.97	2.03	119.9	119.5
$[Zn(NH_3)_4]^{2+}$	16.75	15.3	2.02	2.09	109.5	109.4
			Zn−S			
$[Zn(SH)]^+$	18.06	18.35	2.03	2.18		
$Zn(SH)_2$	27.81	27.56	2.21	2.19	177.5	178.4

3.5. Modeling Zinc in Biological Systems. As a first step toward validating the parameters for Zn-containing biomolecules, we simulated small zinc complexes with NH_3 and SH^- ligands and found a reasonable agreement between our SCC-DFTB and B3LYP results (Table 5). We also reproduced recent B3LYP geometry parameters for cyclic ZnC_n ($n = 2-5$) clusters[51] and found the errors in the Zn−C and C−C bonds to be smaller than 0.05 Å in all cases.

By applying the procedure suggested by Elstner et al.,[19] we calculated three zinc-containing complexes to model zinc interactions with specific functional groups in proteins, using SH^-, CH_2═NH, and $HCOO^-$ ligands to represent the thiol

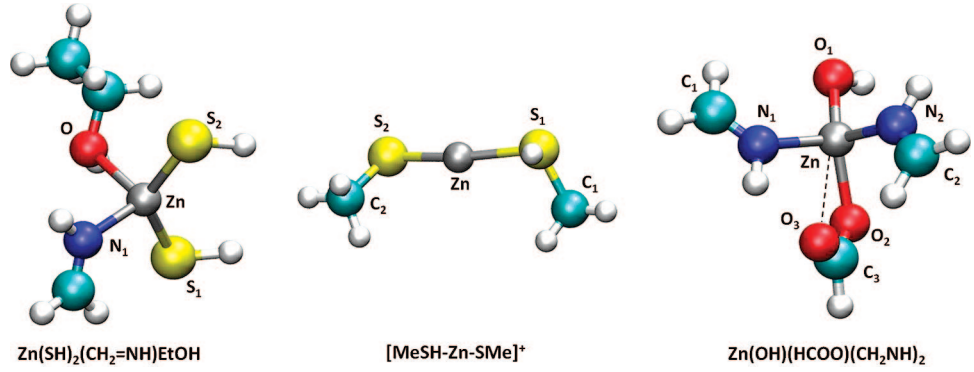

Figure 10. Optimized geometries of model zinc complexes calculated with SCC-DFTB.

Table 6. Comparison of Geometric Parameters of Model Zinc Complexes Calculated with B3LYP/6-311+G(d,p) and SCC-DFTB Methods[c]

	method		
complex	B3LYP[a]	SCC-DFTB[a]	SCC-DFTB[b]
1: $Zn(SH)_2(CH_2{=}NH)EtOH$			
$r(Zn-S_1)$	2.261	2.258	2.301
$r(Zn-S_2)$	2.261	2.243	2.290
$r(Zn-O)$	2.272	2.288	2.158
$r(Zn-N)$	2.155	2.056	2.001
$\angle(S_1-Zn-S_2)$	143.5	140.3	134.0
$\angle(S_2-Zn-O)$	91.2	102.8	105.4
$\angle(S_1-Zn-N)$	106.9	104.1	105.4
2: $[MeSH-Zn-SMe]^+$			
$r(Zn-S_1)$	2.349	2.293	2.329
$r(Zn-S_2)$	2.152	2.123	2.169
$r(S_1-C)$	1.853	1.832	1.831
$\angle(C-S_1-Zn)$	104.9	108.0	104.9
$\angle(S_1-Zn-S_2)$	175.1	169.1	169.9
$\angle(Zn-S_2-C)$	105.8	110.2	105.5
3: $Zn(OH)(HCOO)(CH_2{=}NH)_2$			
$r(Zn-O_1)$	1.876	1.906	1.868
$r(Zn-O_2)$	1.972	2.080	2.023
$r(O_2-C_3)$	1.282	1.301	1.304
$r(C_3-O_3)$	1.237	1.241	1.251
$r(Zn-O_3)$	3.010	2.911	2.931
$r(N_1-C_1)$	1.270	1.267	1.262
$r(Zn-N_2)$	2.129	2.045	2.009
$\angle(O_1-Zn-O_2)$	131.6	109.1	125.8
$\angle(N_1-Zn-N_2)$	103.3	102.7	104.1
$\angle(N_2-Zn-O_1)$	100.3	104.0	109.8

[a] Reference 19. [b] Using current parametrization; this work. [c] Bond lengths are in angstroms, and angles are in degrees.

group in cysteine, the imidazole group in histidine, and the carboxylate group present in all amino acids, respectively. Figure 10 depicts the geometries of the investigated complexes, whereas Table 6 summarizes their geometrical characteristics calculated with B3LYP and two different SCC-DFTB parametrizations (i.e., the current one and that in ref 19). In comparison with DFT results, both DFTB parametrizations describe the Zn−X (X = S, N, O) reasonably well: Zn−S bond lengths in complex **1** were found to be longer by up to 2% compared to DFT ones, whereas the same bonds in complex **2** are described with an accuracy of 0.8% or better with the current parameters. Similar trends were found in the case of Zn−O bond lengths, with errors around 5 and 2.6% in comparison with DFT values for complexes **1** and **3**, respectively. The nonbonded $Zn-O_3$ distance in complex **3** is also in a good agreement with DFT ones (cf. Table 6). The current parametrization leads to underestimation of the Zn−N bond lengths, as exemplified by both complexes **1** and **3** (within 7 and 5.6% differences to DFT, respectively).

Table 7. Comparison of Formation Energies (in Kilocalories per Mole) of Model Zinc Complexes Calculated with B3LYP/6-311+G(d,p) and SCC-DFTB Methods

	method		
	B3LYP	SCC-DFTB[a]	SCC-DFTB[b]
reaction 1[c]	−14.7[d]	−12.3	−20.1
reaction 2[e]	−50.9[f]		−53.2
reaction 3[g]	−159.4[d]	−180.9	−186.9

[a] Reference 19. [b] Using current parametrization; this work. [c] (EtOH) + $Zn(SH)_2(CH_2{=}NH)$ → $Zn(SH)_2(CH_2{=}NH)$ (EtOH). [d] B3LYP/6-311+G(d,p) data from ref 19 (see the supporting materials to the article in ref 19). [e] CH_3SH + $[Zn(SCH_3)]^+$ → $[MeSH-Zn-SMe]^+$. [f] This work. [g] OH^- + $[Zn(HCOO)(CH_2{=}NH)_2]^+$ → $Zn(OH)(HCOO)(CH_2{=}NH)_2$.

Also, the bond angles are reasonably described with both DFTB parametrization. Our S−Zn−S values in complexes **1** and **2**, for instance, agree within 6.6 and 3.3%, respectively, in comparison with DFT results. It should be noted that some bond angles disagree even up to 10° with DFT, which may indicate a relatively floppy bending potential-energy profile.

Table 7 lists formation energies of complexes under study calculated as the difference between the total energy of the complex and those of reactants. It can be inferred from these data that the current SCC-DFTB parametrization leads to an overbinding of ligands in zinc complexes with the largest error to DFT of 0.3 eV (37%) for the first reaction, and 0.1 eV (4.5%) and 1.2 eV (17.2%) for the second and third reaction, respectively. This finding is, however, in line with the general overbinding trend of the DFTB method, and one can safely conclude that the current parametrization is equally applicable to model zinc in biological environment and solid-state systems.

4. Conclusions

In this work, we presented a new SCC-DFTB parametrization for Zn−X interactions (X = H, C, N, O, S, and Zn), which demonstrated a reliable performance in representing the zinc-containing systems, including bulk phases (hcp-Zn, w-ZnO, and zb-ZnS), ZnO surfaces (clean and with adsorbates), ZnO nanostructures, and model zinc biomolecules. Our results indicate that this new set is universal, being transferable

among several different chemical environments, and aims to be a promising computational approach for future in-depth explorations of the properties of complex zinc-containing systems (e.g., ZnO-based hybrid materials or active sites of enzymes).

Acknowledgment. This work was supported by the DFG Priority Program SPP-1165 and by the DIP-40100474. We thank Christof Köhler, Thomas Niehaus, and Simone Sanna for fruitful discussions.

References

(1) Law, M.; Greene, L. E.; Johnson, J. C.; Saykally, R.; Yang, P. *Nat. Mater.* **2005**, *4*, 455–459.

(2) Li, Y.; Meng, G. W.; Zhang, L. D.; Phillipp, F. *Appl. Phys. Lett.* **2000**, *76*, 2011–2013.

(3) Wang, X.; Song, J.; Li, P.; Ryou, D. R.; Dupuis, H. J.; Summers, C. J.; Wang, Z. L. *J. Am. Chem. Soc.* **2005**, *127*, 7920–7923.

(4) Hughes, W. L.; Wang, Z. L. *Appl. Phys. Lett.* **2005**, *86*, 043106.

(5) Wen, X. G.; Fang, Y. P.; Pang, Q.; Yang, C. L.; Wang, J. N.; Ge, W. K.; Wong, K. S.; Yang, S. H. *J. Phys. Chem. B* **2005**, *109*, 15303–15308.

(6) Pan, Z. W.; Dai, Z. R.; Wang, Z. L. *Science* **2001**, *291*, 1947–1949.

(7) Xu, X. Y.; Zhang, H. Z.; Zhao, Q.; Chen, Y. F.; Xu, J.; Yu, P. D. J. *J. Phys. Chem. B* **2005**, *109*, 1699–1702.

(8) Tian, Z. R.; Voigt, J. A.; Mackenzie, B.; Mcdermott, M. *J. Am. Chem. Soc.* **2002**, *124*, 12954–12955.

(9) Lui, R.; Vertegel, A. A.; Bohannan, E. W.; Sorenson, T. A.; Switzer, J. A. *Chem. Mater.* **2001**, *13*, 508–512.

(10) Tian, Z. R.; Voigt, J. A.; Mackenzie, B.; Mcdermott, M.; Rodrigues, M. A.; Konishi, H.; Xu, H. *Nat. Mater.* **2003**, *2*, 821–826.

(11) Taratula, O.; Galoppini, E.; Wang, D.; Chu, D.; Zhang, Z.; Chen, H.; Saraf, G.; Lu, Y. *J. Phys. Chem. B* **2006**, *110*, 6506–6515.

(12) Xu, H.; Zhang, R. Q.; Zhang, X.; Rosa, A. L.; Frauenheim, Th. *Nanotechnology* **2007**, *18*, 485713.

(13) Kohan, A. F.; Ceder, G.; Morgan, D.; Van der Walle, C. G. *Phys. Rev. B* **2000**, *61*, 15019–15027.

(14) Porezag, D.; Frauenheim, Th.; Köhler, Th.; Seifert, G.; Kaschner, R. *Phys. Rev. B* **1995**, *51*, 12947–12957.

(15) Seifert, G.; Porezag, D.; Frauenheim, Th. *Int. J. Quantum Chem.* **1996**, *58*, 185–192.

(16) Niehaus, Th.; Suhai, S.; DellaSala, F.; Lugli, P.; Elstner, M.; Seifert, G.; Frauenheim, Th. *Phys. Rev. B* **2001**, *63*, 085108.

(17) di Carlo, A.; Gheorghe, M.; Lugli, P.; Sternberg, M.; Seifert, G.; Frauenheim, Th. *Physica B* **2002**, *314*, 86–90.

(18) Hohenberg, P.; Kohn, W. *Phys. Rev. Lett.* **1964**, *136*, B864.

(19) Elstner, M.; Cui, Q.; Munih, P.; Kaxiras, E.; Frauenheim, T.; Karplus, M. *J. Comput. Chem.* **2003**, *24*, 565–581.

(20) Seifert, G. *J. Phys. Chem. A* **2007**, *111*, 5609–5613.

(21) Elstner, M.; Porezag, D.; Jungnickel, G.; Elsner, J.; Haugk, M.; Frauenheim, Th.; Suhai, S.; Seifert, G. *Phys. Rev. B* **1998**, *58*, 7260–7268.

(22) Perdew, J. P.; Burke, K.; Ernzerhof, M. *Phys. Rev. Lett.* **1996**, *77*, 3865–3868.

(23) Soler, J. M.; Artacho, E.; Gale, J. D.; García, A.; Junquera, J.; Ordejón, P.; Sánchez-Portal, D. *J. Phys.: Condens. Matter* **2002**, *14*, 2745–2779.

(24) Troullier, N.; Martins, J. L. *Phys. Rev. B* **1991**, *43*, 1993–2006.

(25) Lee, C.; Yang, W.; Parr, R. G. *Phys. Rev. B* **1993**, *37*, 785–789.

(26) Becke, A. D. *J. Chem. Phys.* **1988**, *88*, 1053–1062.

(27) Frisch, M. J.; Trucks, G. W.; Schlegel, H. B.; Scuseria, G. E.; Robb, M. A.; Cheeseman, J. R.; Montgomery, J. A., Jr.; Vreven, T.; Kudin, K. N.; Burant, J. C.; Millam, J. M.; Iyengar, S. S.; Tomasi, J.; Barone, V.; Mennucci, B.; Cossi, M.; Scalmani, G.; Rega, N.; Petersson, G. A.; Nakatsuji, H.; Hada, M.; Ehara, M.; Toyota, K.; Fukuda, R.; Hasegawa, J.; Ishida, M.; Nakajima, T.; Honda, Y.; Kitao, O.; Nakai, H.; Klene, M.; Li, X.; Knox, J. E.; Hratchian, H. P.; Cross, J. B.; Bakken, V.; Adamo, C.; Jaramillo, J.; Gomperts, R.; Stratmann, R. E.; Yazyev, O.; Austin, A. J.; Cammi, R.; Pomelli, C.; Ochterski, J. W.; Ayala, P. Y.; Morokuma, K.; Voth, G. A.; Salvador, P.; Dannenberg, J. J.; Zakrzewski, V. G.; Dapprich, S.; Daniels, A. D.; Strain, M. C.; Farkas, O.; Malick, D. K.; Rabuck, A. D.; Raghavachari, K.; Foresman, J. B.; Ortiz, J. V.; Cui, Q.; Baboul, A. G.; Clifford, S.; Cioslowski, J.; Stefanov, B. B.; Liu, G.; Liashenko, A.; Piskorz, P.; Komaromi, I.; Martin, R. L.; Fox, D. J.; Keith, T.; Al-Laham, M. A.; Peng, C. Y.; Nanayakkara, A.; Challacombe, M.; Gill, P. M. W.; Johnson, B.; Chen, W.; Wong, M. W.; Gonzalez, C.; Pople, J. A. Gaussian 03, revision B.04; Gaussian, Inc.: Wallingford, CT, 2004.

(28) Monkhorst, H. J.; Pack, J. D. *Phys. Rev. B* **1976**, *13*, 5188–5192.

(29) Aradi, B.; Hourahine, B.; Frauenheim, Th. *J. Phys. Chem. A* **2007**, *111*, 5678–5684.

(30) Steinberg, D. J. *J. Phys. Chem. Solids* **1982**, *43*, 1173–1175.

(31) Desgreniers, S. *Phys. Rev. B* **1998**, *58*, 14102–14105.

(32) Ghosh, G.; Delsante, S.; Borzone, G.; Asta, M.; Ferro, R. *Acta Mater.* **2006**, *54*, 4977–4997.

(33) Weiss, R. J.; Mazzone, G. *J. Appl. Crystallogr.* **1981**, *14*, 401–416.

(34) Li, C.; Guo, W.; Kong, Y.; Gao, H. *Phys. Rev. B* **2007**, *76*, 035322.

(35) Jaffe, J. E.; Snyder, J. A.; Lin, Z.; Hess, A. C. *Phys. Rev. B* **2000**, *62*, 1600–1665.

(36) Martins, L. J.; Troullier, N. *Phys. Rev. B* **1991**, *43*, 2213–2217.

(37) Sahraoui, F. A.; Zerroug, S.; Louail, S.; Maouche, D. *Mater. Lett.* **2007**, *67*, 1978–1981.

(38) Koskinen, P.; Hakkinen, H.; Seifert, G.; Sanna, S.; Frauenheim, Th.; Moseler, M. *New J. Phys.* **2006**, *8*, 9.

(39) Meyer, B.; Marx, D. *Phys. Rev. B* **2003**, *67*, 035403.

(40) Claeyssens, F.; Freeman, C. L.; Allan, N. L.; Sun, Y.; Ashfold, N. R.; Harding, J. H. *J. Mater. Chem.* **2005**, *15*, 139–148.

(41) Tusche, C.; Meyerheim, H. L.; Kirschner, J. *Phys. Rev. Lett.* **2007**, *99*, 026102.

(42) Fan, W.; Xu, H.; Rosa, A. L.; Frauenheim, Th.; Zhang, R. Q. *Phys. Rev. B* **2007**, *76*, 073302.

(43) Wander, A.; Harrison, N. M. *J. Phys. Chem. B* **2001**, *105*, 6191–6193.

(44) Nakatsuji, H.; Fukunishi, Y. *Int. J. Quantum Chem.* **1992**, *42*, 1101–1114.

(45) Zapol, P.; Jaffe, J. B.; Hess, A. C. *Surf. Sci.* **1999**, *422*, 1–7.

(46) Wang, Y.; Kovacik, R.; Meyer, B.; Kotsis, K.; Stodt, D.; Staemmler, V.; Qiu, H.; Traeger, F.; Langenberg, D.; Muhler, M.; Wöll, C. *Angew. Chem., Int. Ed.* **2007**, *46*, 5624–5627.

(47) Meyer, B.; Rabaa, H.; Marx, D. *Phys. Chem. Chem. Phys.* **2006**, *8*, 1513–1520.

(48) Law, J. B. K.; Thong, J. T. L. *Nanotechnology* **2008**, *19*, 205502.

(49) Martins, J. B. L.; Longo, E.; Salmon, O. D. R.; Espinoza, V. A. A.; Taft, C. A. *Chem. Phys. Lett.* **2004**, *400*, 481–486.

(50) Ozawa, K.; Hasegawa, T.; Edamoto, K.; Takahashi, K.; Kamada, M. *J. Phys. Chem. B* **2002**, *106*, 9380–9386.

(51) Barrientos, C.; Retondo, P.; Largo, A. *J. Chem. Theory Comput.* **2007**, *3*, 657–664.

CT800455A